Aortic arch morphogenesis and flow modeling in the chick embryo

Yajuan Wang[1], Onur Dur[1], Michael J. Patrick[2], Joseph P. Tinney[3], Kimimasa Tobita[3,4], Bradley B. Keller[1,3,4], Kerem Pekkan[1]

[1]Department of Biomedical and Mechanical Engineering and [2]Molecular Biosensor and Imaging Center, Carnegie Mellon University, Pittsburgh, PA, USA

[3]Departments of Pediatrics and [4]Bioengineering, University of Pittsburgh, Pittsburgh, PA, USA

Running Title:

Embryonic aortic arch morphogenesis and CFD

Address for Correspondence:

Kerem Pekkan, PhD.

Assistant Professor – Biomedical & Mechanical Engineering

Carnegie Mellon University

2100 Doherty Hall, Pittsburgh, PA

Phone: (412) 268 3027

Fax: (404) 268 9807

E-mail: kpekkan@andrew.cmu.edu

Abstract

Morphogenesis of the “immature symmetric embryonic aortic arches” into the “mature and asymmetric aortic arches” involves a delicate sequence of cell and tissue migration, proliferation, and remodeling within an active biomechanical environment. Both patient-derived and experimental animal model data support a significant role for biomechanical forces during arch development. The objective of the present study is to quantify changes in geometry, blood flow, and shear stress patterns (WSS) during a period of normal arch morphogenesis. Composite three dimensional (3D) models of the chick embryo aortic arches were generated at the Hamburger-Hamilton (HH) developmental stages HH18 and HH24 using fluorescent dye injection, micro-CT, Doppler velocity recordings and pulsatile subject-specific computational fluid dynamics (CFD). India ink and fluorescent dyes were injected into the embryonic ventricle or atrium to visualize right or left aortic arch morphologies and flows. 3D morphology of the developing great vessels was obtained from polymeric casting followed by micro-CT scan. Inlet aortic arch flow and body-to-brain flow-split was obtained from 20MHz pulsed Doppler velocity measurements and literature data. Statistically significant variations of the individual arch diameters along the developmental timeline are reported and correlated with WSS calculations from CFD. CFD simulations quantified pulsatile blood flow distribution from the outflow tract through the aortic arches at stages HH18 and HH24. Flow perfusion to all three arch pairs are correlated with the *in vivo* observations of common pharyngeal arch defect progression. The complex spatial WSS and velocity distributions in the early embryonic aortic arches shifted between stages HH18 and HH24, consistent with increased flow velocities and altered anatomy. The highest values for WSS were noted at sites of narrowest arch diameters. Altered flow and WSS within individual arches could be simulated using altered distributions of inlet flow streams. Thus, inlet flow stream distributions, 3D aortic sac and aortic arch geometries, and local vascular biologic responses to spatial variations in WSS are all likely to be important in the regulation of arch morphogenesis.

Keywords

Aortic arches, cardiac development, computational fluid dynamics (CFD), congenital heart disease (CHD), flow visualization, wall shear stress (WSS)

1. Introduction

During embryogenesis, cardiovascular (CV) morphogenesis and adaptation are regulated by both genetic and epigenetic factors, including dynamic three-dimensional (3D) changes in CV structure and function [1, 2]. During embryonic development, *six major pairs of aortic arches (total of 12)* sequentially emerge, remodel, and then disappear, eventually form two mature brachiocephalic arteries (left and right third-derived), an aortic arch (avian: right fourth-derived and human: left fourth-derived) and pulmonary arteries and ductus arteriosus (left and right sixth-derived) [3-5] (Figure 1). Flow-driven hemodynamics plays a significant role in this dynamic process [1, 2, 6], which is clinically described as a "flow-dependency" principle [7-10]. Altered intrauterine hemodynamics during critical windows of cardiac morphogenesis and remodeling leads to congenital arterial defects, such as interruption of aortic arch, double aortic arches, and coarctation of aorta [11, 12]. While the early origins and progression of these defects are well established, little is known regarding the relationships between individual arch geometry and hemodynamics, the distribution of cardiac output through each of the arches, and the influence of altered hemodynamic forces on dynamic arch remodeling.

The avian embryo is an established model for *in vivo* studies that investigate the role of flow-induced mechanical loading on vascular remodeling due to the structural and functional similarities between avian and human hearts [13, 14]. Most investigations of aortic arch structure and function have been limited to ultrasound and contrast imaging [13], which at the moment, provide insufficient morphology and detailed 3D flow information to quantify the biomechanical events that occur during aortic arch remodeling. Several experimental flow visualization techniques including India ink, dye injection [6, 11, 12, 15] and micro particle imaging velocimetry (μPIV) [14, 16, 17] have been used to qualitatively and quantitatively document the hemodynamics in chick normal cardiac development. However, these studies focus primarily on

2D *intra-cardiac* flow patterns and estimate wall shear stress (WSS) through the early tubular heart at Hamburger-Hamilton stage [18] of HH15 and in easily accessible vitelline venous vessels. Limited 3D biomechanical data is available beyond the ventricle and outflow tract. Quantitative 3D imaging using micro-CT has become a standard technique for quantitative 3D reconstruction of complex micro-morphologies including bone [19], vasculature [20] and recently, the developing heart [21]. The initial objective of this research is to establish and validate a multi-modal quantitative approach to investigate and quantify *normal (healthy)* developmental changes of chick embryonic aortic arches in geometry, blood flow and WSS distribution during a period of early development.

Aortic arch hemodynamics has been investigated using computational fluid dynamics (CFD) in the normal mature adult-scale of human aorta [22-24] and in mouse aortic models of atherosclerosis [25-27]. Relevant to patients with congenital heart disease, a patient specific neonatal aortic arch configuration [28] and an *in vitro* experimental and computational study of normal and abnormal embryonic aortic arch hemodynamics at late gestation [29] was published by our group. Compared to the mature systemic aortic arch, the late fetal arch configuration displays relatively complex flow and shear patterns due to the parallel pulmonary and systemic artery flows, and the ductus arteriosus. Given the concurrent changes in cardiac function and aortic arch morphometry that occur during embryogenesis, the current experiments were developed with the anticipation that blood flow and shear stress patterns will be equal or more complex than the case of *late* gestation due to the complex topology of *early* embryonic aortic arches, 3D non-traditional flow characteristics, and dynamic changes in downstream vascular impedance.

In the current era of cardiovascular biology, flow induced changes in cell and tissue biology and architecture are well established as major factors driving the large-scale morphological changes via altered cell proliferation, apoptosis, differentiation, and remodeling. In fetal development, subtle hemodynamic effects could be more striking compared to the mature circulation [30]. With the emergence of fetal intervention strategies to normalize intracardiac blood flow and hemodynamics, there is substantial clinical interest to understand the time course, patterns, and thresholds for shear-stress mediated changes in CV morphogenesis and their relationships to CHD. Major shifts in flow parameters and hemodynamic loads can be calculated using the combination of anatomic, hemodynamic, and CFD data. These data sets can identify unique temporal and spatial windows to guide complementary immunohistochemical and molecular investigations. Therefore, an integrated investigation of the interaction of hemodynamics and developing embryonic aortic arch geometry from mid-to-post cardiac development is described as a first step in acquiring multi-modal data to understand and assess the flow-dependent *in utero* causes (and rationale for potential treatment potentials) of common CHDs.

2. Methods

2.1. Embryo model selection

Fertilized White Leghorn Eggs were studied at Hamburger and Hamilton (HH) Stage 18 (incubation time: 3 days) and Stage 24 (incubation time: 4 days) [18]. Between the selected stages, the aortic arches undergo dramatic structural remodeling, embryonic mass and cardiac output increase fourfold [3, 31]. Embryonic stages are identified by distinguished anatomical differences in limb shape, body curvature and heart anatomy and orientation. At Stage 18, the

heart still maintains its simple smooth transparent tubular topology; whereas for Stage 24, the heart appears trabeculated and started to sink in to the embryo surrounded by semitransparent membranes. Normal embryos were studied acutely at each stage and embryos that were dysmorphic or exhibited overt bleeding were excluded. 111 embryos were used for vascular imaging (n=24 right lateral imaging and n=33 left lateral imaging at Stage 18 and n=30 right lateral imaging and n=24 left lateral imaging at Stage 24).

2.2. India ink and fluorescent dye microinjection

Embryos were incubated at 37°C and 60 to 70% relative humidity to Stage 18, Stage 24 and then exposed by windowing the shell followed by removing the overlying extra embryonic membrane to allow optical access to the embryonic circulatory system. Fluid microinjection was performed using a glass micropipette connected via Silastic tubing to a disposable 22 gauge needle and a 10μl total volume glass Hamilton syringe, mounted in a Leica three-axis micromanipulator. Chick embryos were imaged on either the right side up (right lateral view) or left side up (left lateral view) positions. During normal embryo incubation, 95% of embryos are oriented right-side up and embryos can be carefully manipulated from the right to a left lateral view without altered heart rate or cardiac function [32]. India ink or fluorescent dyes were injected either directly into the ventricular apex or into the atrium while visualizing the embryo in a left-side up orientation. Microinjection volumes ranged from 0.3 to 1.0 μl per injection.

Traditional India ink injection was used to establish basic vascular landmarks including the aortic arches and noted that overlying structures reduced arch flow visualization. Therefore, to improve arch visualization, a variety of water soluble and lipid soluble fluorescent dyes were evaluated, which was provided by Molecular Biosensor and Imaging Center at Carnegie Mellon

University [33, 34] (Figure 2). Fluorescent dyes were diluted at various concentrations using phosphate-buffered saline (PBS) solution. Hydrophilic dyes were well suited to visualize blood flow streams (e.g. Sulforhodamine 101 Free Acid), while hydrophobic dyes penetrated endothelial membranes and labeled most embryonic vessels including the aortic arches (e.g. Rhodamine B, excitation wavelength=550 nm, emission wavelength=570 nm, SPEX industries, Inc., Edison, NJ). For Rhodamine B, image acquisition and camera settings were varied to optimize vascular imaging and an exposure time of 2.35 ms, gamma value of 1.43, and gain of 1.2 were selected. Still frame and time-lapse movies during embryo injection were recorded using a dedicated stereo-dissection/fluorescent microscope (model MZ16F, Leica) suitable for embryo work with either an external normal light source (DCR® III Light Source) or an external fluorescence light source with metal halide bulb (Leica EL6000), and a low light monochrome digital camera (Leica DFC 350FX). Leica imaging software was used to view test images and movies were recorded at frame rates between 6 and 20 frames per second for at least 3 cardiac cycles.

2.3. Aortic arch diameter measurements

Multiple still images were captured throughout the cardiac cycle from both right and left lateral views of the aortic arches at each developmental stage. Aortic arch images were sampled from video images with maximum opacification of the aortic arches, rather than relative to ventricular ejection timing. The diameter of each aortic arch was then measured at the midpoint of the arch between the aortic sac and descending aorta (n=3 measures per vessel). At each measurement location, the maximum possible vessel diameter was verified by acquiring several images

through the vessel z-axis. For the calculation of vessel cross-sectional area and flow rate the arches were assumed to have circular geometry.

2.4. 3D aortic arch imaging and reconstruction

In order to perform CFD simulations, aortic arch 3D geometries were determined by injecting a rapidly polymerizing resin (diluted MICROFIL® Silicone Rubber Injection Compounds MV-blue, Flow Tech Inc, Carver, MA) into the dorsal aorta employing the microinjection set up used for vascular imaging. After microinjection trials using several techniques, it was found that the most reproducible casts were generated by first arresting the embryonic heart in diastole using chick ringer solution with EGTA [35] followed by diluted resin injection (1:7 to 1:12) into the dorsal aorta at Stage 18 and Stage 24, and laceration of the atrium followed by retrograde perfusion via the descending aorta. This protocol worked best at both stages. Higher resin dilution (slower polymerization) was required for the smaller pipette tips and higher resistance of the aortic arches at Stage 18. After resin polymerization, embryos were imbedded in gel (gel base solution: 8ml 30% Acrylamide, 310 μl TEMED, 6ml 3×PBS, 3.7ml D.I. water; 5 drops of 0.02g/ml Ammonium Persulphate) and immersed in isotonic PBS until Micro-CT scanning (Scanco Inc.).

Embryonic aortic arch imaging was performed by acquiring micro-CT DICOM images with standard resolution (~10μm) and 50% overlap. On average, 420 2D images were acquired for each embryo. Image stacks (2D) were pre-processed using DicomWorks (a free DICOM viewer, Lyon, France) to optimize image contrast without altering vessel geometries or dimensions and then image reconstruction (3D) was performed using Simpleware-ScanIP (Simpleware Ltd. Innovation Centre, UK) software. Fluorescent dye injection movies and 3D

reconstructions were overlapped to confirm accurate arch reconstruction. Several representative aortic arch models were selected for each stage and then imported into Geomagics (Geomagic Inc., Durham, NC) to create smooth inflow/outflow boundaries required for computational fluid dynamics analysis. This 3D reconstruction protocol has been partially employed in earlier studies on macro-scale complex anatomies [36, 37]. The current morphology database contained 63 reconstructions from 20 normal embryos for Stage18, Stage 21 and Stage 24.

2.5. CFD simulation and analysis

A mesh sensitivity study was conducted to investigate the effects of both surface and core mesh refinements. A total of 9 auxiliary CFD simulations were performed for each development stage corresponding to coarse, medium and fine surface and volume grid levels. Mesh independent solutions were obtained using approximately 600,000 tetrahedral elements at each stage. Mesh generation was performed using Gambit (ANSYS Inc). A pulsatile 2^{nd} Order CFD solver (Fluent 6.3.26, ANSYS Inc.) originally developed for complex subject-specific anatomical flows was utilized [29, 38]. This experimentally validated model incorporated an implicit pressure based numerical method, high-order discretization schemes, and a robust pressure-correction algorithm to sequentially solve the pressure continuity and the linearized momentum equations assuming incompressible and Newtonian blood flow with constant hemodynamic properties (ρ = 1060 kg/m^3, $\mu = 3.71 \times 10^{-3}$ Pa). The Newtonian assumption is justified for embryonic blood flows having “nucleated” and non-aggregated rigid red blood cells [39]. Vessel walls were assumed to be rigid and impermeable with no slip boundary conditions. Flow split boundary conditions were applied on extended outlets (i.e. approximately 10 vessel diameters). The total cardiac output was distributed to dorsal aorta and cranial vessels with a ratio of 90:10. This outlet boundary

condition strategy allowed the flow to reach the fully developed regime at the distal outlets and ensured a robust convergence of flow and pressure field inside the domain. Pulsatile flow waveforms were selected from our previously published studies (Figure 3) [40] as plug-flow inflow boundary conditions for Stage 18 and Stage 24 [31].

Steady-state solutions were used to initialize the flow field prior to transient solutions. Convergence was enforced by reducing the residual of continuity equation by 10^{-6} at all time steps. Flow variables were monitored in real-time at the aortic inlet and descending aorta outlet during the course of each solution to ensure that nonlinear start-up effects were eliminated. Simulations were continued through six cardiac cycles when the solution became periodic in all models. Computations took approximately 48 hours to complete (one converged cycle with a period of ~0.4 seconds) using a Linux work station with two Quad Core Intel Xeon Processors (8 nodes each 2.66GHz) with 8GB of shared parallel memory.

2.6. Statistical analysis

Data was summarized as mean ± standard deviation (Table 1) and analyzed using repeated measures ANOVA to identify relationships between development stage, arch side (Left/Right), arch number (II^{nd} ,III^{rd}, IV^{th}, VI^{th}) and arch diameter. For the III^{rd} an IV^{th} aortic arches, no significant effect was noted for the interaction of three factors ($p=0.666$) using ANOVA general linear model, and pairwise comparisons were performed on the data followed by Tukey post-hoc analysis. All the data was segregated according to different combinations of variables (development stage and type of aortic arches; development stage and lateral; lateral and type of aortic arches). One way ANOVA was then applied to the data subgroups. Statistical significance was defined at 5% alpha error between groups for a single measure ($p<0.05$).

3. Results

3.1. 3D geometry of the aortic arches

Arch Distribution: From Stage 18 to Stage 24, the number and dimension of embryonic aortic arches on each lateral change dynamically, consistent with increasing cardiac output. At Stage 18 and Stage 24, three pairs of aortic arches were noted in almost all embryos. At Stage 18, left side, only 4 out of 33 embryos had two aortic arches. At Stage 18, right side, all 23 embryos studied had three aortic arches. And at Stage 24 both left (n=24) and right (n=30) sides had three aortic arches. At Stage 18, the three symmetric pairs of aortic arches were identified as the IInd, IIIrd and IVth arches, and based on fluorescence intensity; the IIIrd aortic arches received the most flow. At Stage 24, the IInd aortic arches were no longer visible and the arch pattern transformed into the IIIrd, IVth and VIth arches. Including the interim Stage 21 data (not shown here), it is observed that 3-arch pair pattern moved from anterior to posterior through sequential vessel formation and extinction. As the aortic sac and arches remodel, the common outflow tract and aortic sac was noted to maintain alignment with the middle aortic arches at Stages 18 and 24.

Arch Dimensions: The mean dimension of the individual aortic arch varied between the right and left sides and with development. The distribution and relative diameters of the IInd, IIIrd, IVth and VIth right and left aortic arches are shown in Table 1. Both the differences in the diameters of right and left similar numbered arches and the distribution of the arches varied from Stage 18 to Stage 24. For example, at Stage 18, the right and left IIIrd aortic arches were larger than the other two pairs and the IVth arches had smallest diameter ($p<0.001$). The average arch diameter from Stage 18 to Stage 24 showed a right dominant trend, consistent with the avian mature right dominant aortic arch (Stage 24: IIIrd pairs: $p=0.014$; IVth pairs: $p=0.001$; VIth pairs:

$p<0.001$). From Stage 18 to Stage 24, we found that the diameters of the left IIIrd arches decreased ($p=0.007$); while the diameters of the IVth (right: $p<0.0001$, left: $p<0.0001$) increased. There was no statistical difference in Right IIIrd arch diameter between Stage 18 and 24 ($p=0.389$).

3D Arch Topology: The embryonic heart tube continues to undergo cardiac looping between Stage 18 and Stage 24, shifting the positions of both the outflow tract and the aortic sac relative to the ventricles. At Stage 18, the outflow tract is predominantly right sided and then remodels to a more midline location by Stage 24. This shift in outflow tract position was accompanied with the disappearance of IInd aortic arches, emergence of VIth aortic arches and shifts in the dimension of the IIIrd and IVth aortic arches. With the increase of the angle between the branches of two cranial arteries, the aortic arch pairs displayed increasing curvature. Meanwhile, the curvature of dorsal aorta also increased as the two cranial arteries extended towards the head. The progressive narrowing between the junction of cranial arteries and the paired dorsal aorta eventually leads to a separation of the IIIrd aortic arches from the dorsal aorta and their direct connection to the cranial arteries.

3.2. 3D flow pattern in the aortic arch manifold

Blood flow through specific aortic arches was simulated and tracked through the cardiac cycle using the CFD results of representative 3D composite reconstructions. In this manuscript, the flow distributions were presented for Stage 18 and Stage 24. The distribution of cardiac output through each of the individual arch vessels are investigated through the quadrant flow analysis technique. The cross section of the outflow tract (inflow to the aorta) was segmented into four quadrants and pulsatile flow path-lines initiating from these quadrants were labeled with four

different colors to represent specific pathways through the aortic sac and individual arch segments (Figure 4 and Figure 5).

At Stage 18, blood from the upper left quadrant (green) and upper right quadrants (blue) preferentially perfused the left sided arches while blood from the lower right quadrant (pink) and lower left quadrants (orange) preferentially perfused the right sided arches (Figure 4). Stage 18 upper left quadrant flow (green) distributed through the lower lumen of left IInd aortic arch, the whole lumen of left IIIrd aortic arch, the upper lumen of left IVth aortic arch and also inner curve of right IIIrd aortic arch. Stage 18 lower left quadrant flow (blue) distributed predominantly through the paired IVth aortic arches. Stage 18 lower right quadrant flow (orange) distributed mainly through the right IIIrd aortic arch and partial lumen of right IVth aortic arch. Stage 18 upper right quadrant flow (pink) distributed predominantly through the nearby right IInd and IIIrd aortic arches, while a small amount of flow perfused the left IInd aortic arches and then the left cranial arteries. Flow from the right IInd aortic arch entered both the right cranial artery and right sided dorsal aorta. These results predict that blood from three quadrants (upper left, lower right and lower left,) perfuse the IIIrd aortic arch pairs which are dominant at this stage.

At Stage 24 (Figure 5), aortic sac inlet blood flow distribution had a similar distributed effect on regional aortic arch perfusion; however, due to changes in the aortic sac orientation and aortic arch geometry, the perfusion pattern was considerably different from Stage 18. Blood from the upper left quadrant (green) filled the upper lumen of right IIIrd, the whole lumen of left IIIrd and upper lumen of left IVth aortic arches. At the junction of the IIIrd aortic arches, cranial arteries and dorsal aorta, the streamlines diverged between the cranial arteries and the dorsal aorta leading to a predictable site of increased wall shear stress. Blood from lower left (blue) and lower right (orange) quadrants at Stage 24 provided increased flow to more arches versus Stage

18. Blood from lower left quadrant (blue) perfused the lower lumen of right IIIrd, the lumen of right IVth, VIth and also left VIth aortic arches, while blood from lower right quadrant (orange) perfused the right IIIrd, left IIIrd, IVth and VIth aortic arches. Blood from the upper right quadrant (pink) perfused the lower lumen of right IIIrd and upper lumen of right IVth aortic arches. Most of this upper right stream consequently converged into dorsal aorta with only a small amount perfusing the cranial arteries (in contrast to the greater cranial perfusion provided by the comparable quadrant at Stage 18).

Of note, the particle path-line distribution patterns did not vary substantially throughout the acceleration and deceleration phases of the cardiac cycle (for the entire cardiac cycle patterns, see the Supplementary Movie for Stage 24) and identical to the mean flow streamline patterns. This is expected due to the low Reynolds number flow regime with limited convective mixing. For Stage 18, the maximum velocity in model was 0.17 m/s at the inlet aortic and Reynolds (Re) numbers were approximately 4. For Stage 24, the maximum velocity recorded in aortic arches was 0.25 m/s at convergence sites of cranial arteries and dorsal aorta. Re numbers were approximately 25 at the inlet aortic sac. For both stages, the Womersley number (α) were smaller than 1.

3.3. Wall shear stress distribution

Wall shear stress (WSS) distribution for Stage 18 left and right sided aortic arches at the acceleration, peak, and deceleration phases are displayed in Figure 6 a-c and in Table 2. It is noted that high WSS appeared at locations where flow converged and at narrow arch locations at Stage 18. The maximum WSS value was 687 dynes cm^{-2} located at the transition between the aortic sac and the aortic arches during peak flow phase. WSS distributions for Stage 24 left and

right-sided aortic arches at the acceleration, peak, and deceleration phases are displayed in Figure 7 a-c. Aortic arch WSS at Stage 24 displayed more sites of high WSS (>105 dynes cm^{-2}) including the aortic sac outlet, narrow midpoints of the left IV^{th} and right VI^{th} aortic arches and at the junctions of paired III^{rd} arches with the cranial arteries and dorsal aorta. The maximum WSS value at Stage 24 was 720 dynes cm^{-2} located at the narrow midpoint of the left IV^{th} aortic arch at the peak flow.

Non-parametric pair-wise comparison of WSS over the III^{rd} and IV^{th} aortic arches at Stages 18 and 24 reveals that both the time-averaged and peak-flow WSS increases ($p = 0.0078$) across-stages (Table 2). Increased WSS corresponds to increased cardiac output at Stage 24 relative to Stage 18. Contours of WSS displayed large spatial variations axially along the arch centerline due to the sudden regression in vessel caliper (see left IV^{th} and right VI^{th} aortic arches in Figure 6 and 7).

In addition, across-stages variation of aortic arch diameters correlated with the variation of time-averaged WSS at the corresponding locations ($p<0.015$). Of note, increase in the midpoint diameter of the right IV^{th} arch is (statistically more significant ($p<0.0001$)) and quantitatively largest (+0.057mm) compared to across-stage diameter variation of the other arches (Table 2). Hence, the transitions in arch diameters are consistent with expansion of the "dominant" right IV^{th} avian aortic arch, which forms the mature aorta, correlated strongly with the variation in the hemodynamic loading.

4. Discussion

4.1. Tracking intra-cardiac flow patterns beyond the ventricle

The exact number of distinct intracardiac flow streams that exist in the developing heart (sustained by the low Reynolds number flow regimes) and their role in regulating the morphogenesis of spiral aorto-pulmonary septum has long been debated [41, 42]. Since the 1960s, India ink and other dye tracers have been employed systematically to understand this important flow structure. Leyhane used methylene blue to track blood flow from right or left vitelline vein and visualized the distinct currents in chick embryos from Stage 17 to Stage 19 [43]; Yoshida et al. used the same methods and found two flow stream patterns in the embryonic heart and aortic arch [15]. A contemporary investigation by Hogers et al. documented the intracardiac flow patterns of normal and experimentally altered chick embryos (such as right, left or posterior vitelline vein ligation) after injecting India ink into tributaries of the vitelline system at different yolk sac sites [6, 11, 12]. These studies have provided sufficient qualitative evidence that cardiac morphology and function is impacted by altered flow patterns. Earlier studies relied on the 2D optical projections of streamlines, and the quantification of flow data beyond the outflow tract was limited due to the 3D morphology of the aortic arches and their tendency for increasingly limited optical access with development. The 3D pulsatile CFD results presented in this manuscript enabled for the first time in the literature the quantitative tracking of the intra-cardiac flow currents beyond the ventricle and the specific aortic arch lumen at early (Stage 18) and later stages (Stage 24).

Previous in vivo studies performed by Hogers et al. confirmed the presence of unique intracardiac flow streams which originate from different yolk sac regions (right lateral, left lateral, anterior and posterior) and distribute equally in four quadrants along the cross section of

the conotruncus (inlet of the aortic sac) [6]. Selective reduction of these flow streams due to the viteline vein ligation results in significant shifts in the normal quadrant flow pattern and is associated with downstream pharyngeal arch artery malformations including an interrupted aorta, reduced diameter of the right third or sixth pharyngeal arch arteries and in some cases an additional left aorta [12]. The orientations of the quadrants adopted in this analysis (Section 3.2) were guided by this earlier study which enabled the tracking of the abnormal flow streams through the aortic sac and specific arches. Hogers et al. (1995) showed that after right vitelline vein ligation at Stage 17, embryonic blood flow concentrates in ventral right quadrants and a small portion of the ventral left quadrants of the cross section of conotruncus [6]. Results of this study indicate that this disturbed quadrant blood flow pattern would lead to reduced right II^{nd}, III^{rd} and both IV^{th} aortic arch perfusion but more blood flow in the II^{nd}, III^{rd} and left IV^{th} aortic arches. Interestingly for certain arches, their eventual re-distribution of blood flow is dependent upon dual altered flow patterns due to a compromise between lesser perfusion possibility of inlet quadrants and more flow mass perfusion of certain aortic arch systems. This could explain the in vivo observation that ligation of right vitelline vein results in two distinct outcomes, e. g. the interruption of aorta and the generation of double aortic arch in Hogers' observation. Results of this study confirm that altered local perfusion of aortic arch impacts the terminal congenital morphologies. Further prognosis of this intervention can be studied with this composite model at Stage 24, which could simulate the blood streamlines in specific aortic arches at this stage as well. The present analysis is applicable to other possible embryonic interventions, performed either to create or to treat congenital heart defects, and the effect of altered aortic arches perfusion can be investigated.

4.2. Analysis of WSS distribution

Compared to the human aorta, flow within the aortic arches of smaller animals results in a lower peak Reynolds numbers and considerably higher wall shear stresses [25, 44]. Earlier CFD studies indicated complex characteristic WSS distributions proximal to the vessel anastomosis regions. In spite of the more complex arch manifold, the present study followed the similar trend of higher WSS in even smaller body sizes and complex regional differences. This trend implies that during development the absolute value of WSS could be selectively interpreted and associated with diverse endothelial functions. At Stage 24, the higher time-averaged WSS is located on the right IVth aortic arch coinciding with significantly larger vessel diameters, indicating that this level of WSS (28 dynes cm^{-2}) results in cell proliferation for this region [45]. While an order of magnitude higher WSS value at the junction of IIIrd aortic arches, cranial arteries and dorsal aorta could trigger the regression of these regions interfering with the apoptosis pathway. Aside from the magnitude of WSS, the dynamics of WSS (oscillatory, unidirectional, etc.) is another possible factor for functional differentiation [46, 47].

Changes in WSS clearly trigger altered endothelial cell function and gene expression [2]. The majority of previous in vitro studies conducted at lower WSS levels in mature vascular systems demonstrate that endothelial cells are sensitive to WSS as low as 1 dynes cm^{-2} [48]. The WSS levels considerably larger than 1 dynes cm^{-2}, as found in present models, not only suggest that the WSS exerted by blood flow can be sensed (by endothelial cell and then stimuli a gene expression pathway to change the macro morphology and function) but also that the WSS sensitivity of the developing endothelium can be continuously adapting to the changing mean WSS level. This can be an indicator of the developmental time points transmitted to the gene program. The extent of this mechanism at considerably higher WSS levels as observed in the

developing embryo becomes critical and requires more investigation at higher WSS levels. The 3D expression of shear stress responsive genes, KLF-2, ET-1 and NOS-3 in the developing cardiovascular system of chick embryos were recently investigated where KLF-2 and NOS-3 levels were known to be elevated at the high shear sites of Stage 18 [1, 49-51]. These studies also suggested that the vascular malformations created by right vitelline vein ligation are associated with the ET-1 pathway. Likewise, the high WSS regions calculated in this study predict enhanced KLF-2 and NOS-3 expression at these areas which are in qualitative agreement with the 3D gene expression patterns detected in Gittenberger-de Groot and Robert E. Poelmann [49], including the maximum shear stress region of the inlet aortic sac where larger ET-1 gene expression levels are recorded.

4.3. Verification of the composite 3D models

Limited qualitative information on the 3D morphogenesis of embryonic aortic arches is available from the scanning electron micrograph pictures of vascular casts of chick embryo from Stage 19 to Stage 24 [3]. In addition, Waldo et al. presented the right lateral schematic diagrams of major great vessels at HH Stages 18, 22, 25 [52] and performed preliminary qualitative computational reconstructions from serial registered histological sections of embryonic heart with aortic arches at Stage 18 and Stage 24 [1, 49]. Although 3D information is very limited in these reports, all of these studies are in qualitative agreement with the topology of composite 3D reconstructions in the current study, which were acquired from micro-CT scans. Specific anatomical features such as the complex 3D narrowing of the 3rd aortic arches, cranial arteries and dorsal aorta junction at Stage 24, which will further disconnect from the dorsal aorta at Stage 27, is in agreement with Hiruma et al. [3]. The integrity of the present 3D quantitative morphology of the aortic arch was

further verified; (1) by overlapping the 3D reconstructions with the large set of 2D fluorescence dye injection recordings at several views, (2) through multiple snap-shots used for vessel diameter measurements and (3) by the auxiliary micro-CT scans and 3D reconstructions with parametric segmentation and smoothing settings. Vessel diameter measurements of the individual arches in this study were performed at the mid-point locations to capture the minimum vessel diameter and therefore the greatest hydrodynamic resistance since the formation of aortic arch begins from two ends and eventually connects in the middle [3]. The 3D model agrees well with these 2D results. Detailed statistical analysis was also performed on the measurement results of aortic arch diameters.

4.4. Limitations

The 2D diameter measurements used in the current study were influenced by both reflected fluorescent light and by the volume of injected dye. Therefore large sample numbers were used and a complete statistical analysis was performed to reduce these effects. Since the selection of midpoint and normal direction of the aortic arch was user dependent, a t-test of measurements conducted by different observers need to be performed on the existing time-lapsed fluorescent movie recordings. The vessel wall in this study was assumed to be rigid throughout the cardiac cycle because no significant changes in wall movement were observed distal to the outflow tract. In this study the body-to-head flow split is kept at the physiological well established literature ratio of 90 to 10, while simulations can easily be performed for more balanced flow split ratios with the existing CFD model. Finally, while it is important to interpret the relationships between flow patterns, WSS, gene expression and aortic arch morphology, the inclusion of data related to

hemodynamic factors, such as WSS gradient, oscillatory shear index and other biological assays may be required since the information on the exact bio-physical interaction is still limited.

4.5. Conclusion

Expanding on the previous intra-cardiac hemodynamic investigations, the present study is a first attempt to reconstruct the normal (healthy) micro 3D aortic arch morphology and flow distribution during a critical period of development based on anatomical casts in chick embryo. Several major findings are reported including: (1) Aortic arch patterns change from IInd, IIIrd and IVth to IIIrd, IVth and VIth between Stages 18 and 24; by Stage 24, the mean diameters of the right arches are significantly larger than the left, consistent with the future right dominant arch in avian species; (2) extensive 3D anatomical changes in size, curvature and orientation of the developing arches and cranial vessels are quantified through multiple composite models; (3) differences in flow regimes during development and individual arch flow-splits at healthy conditions are documented which will provide an important baseline data in future studies with congenitally defected models; (4) statistical correlation between flow and morphology indicates that altered blood flow distribution of aortic sac impacts regional aortic arch perfusion and 3D orientation of outflow tract can drive the paired arch growth and regression; and (5) complex and high WSS distributions are found at the bifurcation and stenosed vessel regions with the highest value around 700 dynes cm^{-2} at low Reynolds regimes.

The present results confirm both the importance of blood flow for the normal development and the possibility of selectively regulating the embryonic arch flow split or wall shear stress patterns to intervene and counteract the progressing pharyngeal arch artery malformations.

Acknowledgements

This research is supported by American Heart Association Beginning-Grant-in-Aid 0765284U (PI: Pekkan) and by the Children's Hospital of Pittsburgh Foundation.

Gratitude is expressed to Dr. Arvydas Usas in the micro-CT scanning. Dr. James Fitzpatrick, Dr. Greg Fisher and Dr. Alan Waggoner provided valuable expertise on microscopy and fluorescent dye studies. We also acknowledge Pittsburgh Supercomputing Center grant CCR080013 facilitating high-performance parallel CFD runs presented in this manuscript.

List of Tables

Table 1: Developmental shifts and measurements of the aortic arch mid-point diameters at Stages 18 and 24. L: left; R: right; SD: standard deviation; n: number of samples studied per group. Statistically significant differences ($p<0.05$) in individual arch diameter between stages are denoted by * (arch growth). For fixed arch type, the statistically significant diameter differences between R and L laterals are denoted by † (right dominance). Statistically significant differences from the remaining two arches on the same lateral are indicated by ‡.

Table 2: Wall shear stress (WSS) averaged spatially over each aortic arch segment at Stages 18 and 24 for the peak flow condition and averaged over the cardiac cycle (time-averaged); L: left; R: right; SD: standard deviation. The cardiac-cycle averaged WSS at the midpoint of the arches are also provided for comparison with the measured midpoint diameters (Table 1). WSS for individual arch is calculated from the representative CFD model for Stage 18 and Stage 24.

List of Figures

Figure 1: A cartoon representation of all 6 pairs of aortic arch branches that appear, disappear and reappear during early embryonic development. Not all arches exist at the same time, and a general trend occurs where cranial arches are replaced by caudal arch pairs. The sketch on the right hand side shows the association of major arterial great vessels at term with these six aortic arch pairs. Grey solid lines represent the arch vessels that became extinct during development.

Figure 2: Representative left lateral (a,c) and right lateral (b,d) views of embryonic chick aortic arches with Rhodamine B at Stage 18 (a, b) and Stage 24 (c, d). There are 3 pairs of aortic arches at Stages 18 and 24, but with different patterns. Individual aortic arches are labeled with roman numerals. The scale bar corresponds to 500 μm.

Figure 3: Pulsatile flow rate waveforms used to represent a single cardiac cycle at the inlet to the aortic sac for Stage 18 and Stage 24 models based on the data published by Yoshigi et al. (2000) Ref. [40]. The heart rate is 160 beat per second at Stage 18 and 132 beat per second at Stage 24.

Figure 4: Representative mean flow path-lines at Stage18 of particles released from different inlet quadrants into the proximal aortic sac. Note that flow stream separation was maintained in the aortic sac and each quadrant of inlet flow preferentially filled specific right and/or left aortic arches. Panel a: Right upper quadrant flow or right ventral quadrant flow (pink). Panel b: Left upper quadrant flow or left ventral quadrant (green). Panel c: Right lower quadrant flow or right dorsal quadrant flow (orange). Panel d: Left lower quadrant flow or left dorsal quadrant flow (blue).

Figure 5. Representative mean flow path-lines at Stage 24 of particles released from different inlet quadrants into the proximal aortic sac. Similar to Stage 18, flow stream separation was maintained in the aortic sac and each quadrant of inlet flow preferentially filled specific right and/or left aortic arches, though the pattern differed from Stage 18 due to disappearance of the IInd aortic arches and appearance of the VIth aortic arches. Panel a: Right upper quadrant flow

(pink). Panel b: Left upper quadrant flow (green). Panel c: Right lower quadrant flow (orange). Panel d: Left lower quadrant flow (blue).

Figure 6: Aortic sac and aortic arch wall shear stress (WSS) distributions at Stage 18 displayed from left lateral (L) and right lateral (R) views. Corresponding to (a) flow acceleration; (b) peak flow velocity; (c) flow deceleration phases of the cardiac cycle. A maximum WSS value of 687 dynes/cm^2 was noted briefly in several distinct areas (see arrow). In order to display a broader range of WSS, a peak WSS of 350 dynes/cm^2 is shown in the legend.

Figure 7: Aortic sac and aortic arch wall shear stress (WSS) distributions at Stage 24 displayed from left anterior oblique (L) and right lateral (R) views. Corresponding to (a) flow acceleration; (b) peak flow velocity; (c) flow deceleration. A maximum WSS value of 720 dynes/cm^2 was noted briefly in several distinct areas (see arrow). In order to display a broader range of WSS, a peak WSS of 350 dynes/cm^2 is shown.

References

[1] Poelmann, R. E., A. C. Gittenberger-de Groot, B. P. Hierck, 2008, "The development of the heart and microcirculation: role of shear stress," Med Biol Eng Comput, 46, pp. 479-484.
[2] Hove, J. R., R. W. Koster, A. S. Forouhar, G. Acevedo-Bolton, S. E. Fraser, M. Gharib, 2003, "Intracardiac fluid forces are an essential epigenetic factor for embryonic cardiogenesis," Nature, 421, pp. 172-177.
[3] Hiruma, T., R. Hirakow, 1995, "Formation of the pharyngeal arch arteries in the chick embryo. Observations of corrosion casts by scanning electron microscopy," Anat Embryol, 191, pp. 415-423.
[4] Hiruma, T., Y. Nakajima, H. Nakamura, 2002, "Development of pharyngeal arch arteries in early mouse embryo," J. Anat., 201, pp. 15-29.
[5] Sadler, T. W., 2005, "Langman's Medical Embryology," pp. 159-194.
[6] Hogers, B., M. C. DeRuiter, A. M. J. Baasten, A. C. Gittenberger-de Groot, R. E. Poelmann 1995, "Intracardiac blood flow patterns related to the yolk sac circulation of the chick embryo," Circulation Research, 76, pp. 871-877.
[7] Gardiner, H., J. Brodszki, A. Eriksson, K. Marsál 2002, "Volume blood flow estimation in the normal and growth-restricted fetus," Ultrasound Med Biol, 28(9), pp. 1107-1113.
[8] Rudolph, A. M., M. A. Heymann 1970, "Circulatory changes during growth in the fetal lamb," Circ Res., 26(3), pp. 289-299.
[9] Ursell, P. C., J. M. Byrne, T. R. Fears, B. A. Strobino, W. M. Gersony 1991, "Growth of the great vessels in the normal human fetus and in the fetus with cardiac defects," Circulation, 84(5), pp. 2028-2033.
[10] Zamir, M., P. Sinclair, T. H. Wonnacott 1992, "Relation between diameter and flow in major branches of the arch of the aorta," J Biomech, 25(11), pp. 1303-1310.
[11] Hogers, B., M. C. DeRuiter, A. C. Gittenberger-de Groot, , R. E. Poelmann, 1997, "Unilateral Vitelline Vein Ligation Alters Intracardiac Blood Flow Patterns and Morphogenesis in the Chick Embryo " Circulation Research. , 80, pp. 473-481.
[12] Hogers, B., M. C. DeRuiter, A. C. Gittenberger-de Groot, R. E. Poelmann, 1999, "Extraembryonic venous obstructions lead to cardiovascular malformations and can be embryolethal," Cardiovascular Research, 41, pp. 87-99.
[13] McQuinn, T. C., M. Bratoeva, A. deAlmeida, M. Remond, R. P. Thompson, D. Sedmera, 2007, "High-frequency ultrasonographic imaging of Avian Cardiovascular Development," Developmental Dynamics, 236, pp. 3503-3513.
[14] Peolma, C., P. Vennemann, R. Lindken, J. Westerweel, 2008, "In vivo blood flow and wall shear stress measurements in the vitelline network," Exp Fluids.
[15] Yoshida, H., F. Manasek, R. A. Arcilla, 1983, "Intracardiac flow patterns in early embryonic life. ," Circ. Res., 53, pp. 363-371.
[16] Ravnic, D. J., Y. Z. Zhang, A. Tsuda, J. P. Pratt, H. T. Huss, S. J. Mentzer, 2006, "Multi-image particle tracking velocimetry of the microcirculation using fluorescent nanoparticles," Microvascular Research, 72, pp. 27-33.
[17] Vennemann, P., K. T. Kiger, R. Lindken, B. C. W. Groenendijk, S. Stekelenburg-de Vos, T. L. M. ten Hagen, N. T. C. Ursem, R. E. Poelmann, J. Westerweel, B. P. Hierck, 2006, "In vivo micro particle image velocimetry measurements of blood-plasma in the embryonic avian heart," Journal of Biomechanics, 39, pp. 1191-1200.

[18] Hamburger, V., H. L. Hamilton 1951, "A series of normal stages in the development of the chick embryo," Journal of Morphology, 88(1), pp. 49-92.
[19] Guldberg, R. E., C. L. Duvall, A. Peister, M. E. Oest, A. S. Lin, A. W. Palmer, M. E. Levenston 2008, "3D imaging of tissue integration with porous biomaterials," Biomaterials, 29(28), pp. 3757-3761.
[20] Young, S., Kretlow, J. D., Nguyen, C., Bashoura, A. G., Baggett, L. S., Jansen, J. A., Wong, M., Mikos, A. G., 2008, "Microcomputed Tomography Characterization of Neovascularization in Bone Tissue Engineering Application," Tissue Eng Part B Rev.
[21] Butcher, J., D. Sedmera, R. E. Guldberg, R. R. Markwald, 2006, "Quantitative volumetric analysis of cardiac morphogenesis assessed through micro-computed tomography," Developmental Dynamics, 236(3), pp. 802-809.
[22] Jin, S., J. Oshinski, D. P. Giddens, 2003, "Effects of wall motion and compliance on flow patterns in the ascending aorta," Journal of Biomechanical Engineering, 125, pp. 347-354.
[23] Leuprecht, A., S. Kozerke, P. Boesiger, K. Perktold, 2003, "Blood flow in the human ascending aorta: a combined MRI and CFD study," Journal of Engineering Mathematics 47, pp. 387-404.
[24] Morris, L., P. Delassus, A. Callanan, M. Walsh, F. Wallis, P. Grace, T. McGloughlin, 2005, "3-D numerial simulation of blood flow through models of the human aorta," Journal of Biomechanical Engineering, 127, pp. 767-775.
[25] Feintuch, A., P. Ruengsakulrach, A. Lin, J. Zhang, Y. Q. Zhou, J. Bishop, L. Davidson, D. Courtman, F. S. Foster, D. A. Steinman, R. M. Henkelman, C. R. Ethier 2007, "Hemodynamics in the mouse aortic arch as assessed by MRI, ultrasound, and numerical modeling," American Journal of Physiology - Heart and Circulatory Physiology, 292, pp. H884-H892.
[26] Greve, J. M., A. S. Les, B. T. Tang, M. T. D. Blomme, N. M. Wilson, R. L. Dalman, N. J. Pelc, C. A. Taylor, 2006, "Allometric scaling of wall shear stress from mice to humans: quantification using cine phase-constract MRI and computational fluid dynamics," Am. J. Physiol. Heart Circ. Physiol., 291, pp. H1700-H1708.
[27] Suo, J., D. E. Ferrara, E. Sorescu, R. E. Guldberg, W. R. Taylor, D. P. Giddens, 2007, "Hemodynamic shear stress in mouse aortas implications for atherogenesis," Arterioscler Thromb. Vasc. Biol., 27(346-351).
[28] Pekkan, K., O. Dur, K. Kanter, K. Sundareswaran, M. Fogel, A. Yoganathan, A. Ündar,, 2008, "Neonatal Aortic Arch Hemodynamics and Perfusion during Cardiopulmonary Bypass," Journal of Biomechanical Engineering, in press.
[29] Pekkan, K., L. P. Dasi, P. Nourparvar, S. Yerneni, K. Tobita, M. A. Fogel, B. B. Keller, A. Yoganathan, 2008, "In vitro hemodynamic investigation of the embryonic aortic arch at late gestation," Journal of Biomechanics, 41, pp. 1697-1706.
[30] Hubbard, A. M., and Harty, P., 1999, "Prenatal magnetic resonance imaging of fetal anomalies," Semin Roentgenol, 34(1), pp. 41-47.
[31] Hu, N., E. B. Clark, 1989, "Hemodynamics of the stage 12 to stage 29 chick embryo," Circ Res., 65(6), pp. 1665-1670.
[32] Campbell, K. A., N. Hu, E. B. Clark, B. B. Keller, 1992, "Analysis of dynamic atrial dimension and function during early cardiac development in the chick embryo," Pediatric Research, 32, pp. 333-337.
[33] Mujumdar, R. B., L. A. Ernst, S. R. Mujumdar, C. J. Lewis, A. S. Waggoner, 1993, "Cyanine dye labeling reagents: sulfoindocyanine succinimidyl esters," Bioconjug chem., 4(2), pp. 105-111.

[34] Sims, P. J., A. S. Waggoner, C.-H. Wang, J. F. Hoffman, 1974, "Studies on mechanism by which cyanine dyes measure membrane-potential in red blood-cells and phosphatidylcholine vesicles," Biochemistry, 13(16), pp. 3315-3330.
[35] Taber, L. A., N. Hu, T. Pexieder, E. B. Clark , B. B. Keller 1993, "Residual strain in the ventricle of the stage 16-24 chick embryo. ," Circ Res 72(2), pp. 455-462.
[36] Frakes, D. H., M. J. Smith, J. Parks, S. Sharma, S. M. Fogel, A. P. Yoganathan 2005, "New techniques for the reconstruction of complex vascular anatomies from MRI images," J Cardiovasc Magn Reson, 7(2), pp. 425-432.
[37] Pekkan, K., D. de Zélicourt, L. Ge, F. Sotiropoulos, D. Frakes, M. A. Fogel, A. P. Yoganathan 2005, "Physics-driven CFD modeling of complex anatomical cardiovascular flows-a TCPC case study," Ann Biomed Eng., 33(3), pp. 284-300.
[38] Wang, C., K. Pekkan, D. de Zelicourt, A. Parihar, A. Kulkarni, M. Horner, A. P. Yoganathan 2007, "Progress in the CFD Modeling of Flow Instability in Anatomical Total Cavopulmonary Connections," Annals of Biomedical Engineering, 35(11), pp. 1840-1856.
[39] Dintenfass, L., 1985, Blood Viscosity, Hyperviscosity and Hyperviscosaemia, MTP Press (Kluwer), London.
[40] Yoshigi, M., Knott, G. D., Keller, B. B., 2000, "Lumped parameter estimation for the embryonic chick vascular system: a time-domain approach using MLAB," Computer Methods and Programs in Biomedicine, 63, pp. 29-41.
[41] Schleich, J.-M., Pontchaillou, C. A., Dillenseger, J.-L., and Coatrieux, J.-L., 2002, "Understanding Normal Cardiac Development Using Animated Models," IEEE Computer Graphics and Applications, January/February, pp. 14-19.
[42] Romanoff, A., 1961, Avian Embryo, Structural and Functional Development, Macmillan.
[43] Leyhane, J. C., "Visualization of blood streams in the developing chick heart," Anat. Rec., 163, pp. 312-313.
[44] Huo, Y. X. G., G. S. Kassab, 2008, "The flow field along the entire Length of Mouse Aorta and Primary Branches," Annals of Biomedical Engineering, 36, pp. 685-699.
[45] Ohno, M., Cooke, J. P., Dzau, V. J., and Gibbons, G. H., 1995, "Fluid shear stress induces endothelial transforming growth factor beta-1 transcription and production. Modulation by potassium channel blockade," J Clin Invest, 95(3), pp. 1363-1369.
[46] Himburg H. A., D. S. E., Friedman M. H., 2007, "Frequency-dependent response of the vascular endothelium to pulsatile shear stress.," Am J Physiol Heart Circ Physiol, 293(1), pp. H645-653.
[47] Ziegler T., B. K., Harrison V. J., Brunner H. R., Hayoz D., , 1998, "Influence of oscillatary and unidirectional flow environments on the expression of endothelin and nitric oxide synthase in cultured endothelial cells," Arterioscler Thromb Vasc Biol., 18(5), pp. 686-692.
[48] Even-Tzur, N., Y. Kloog, M. Wolf, D. Elad, 2008, "Mucus secretion and cytoskeletal modifications in cultured nasal epithelial cells exposed to wall shear stresses," Biophysical Journal, doi:10.1529/biophysj.107.127142.
[49] Groenendijk, B. C. W., B. P. Hierck, A. C. Gittenberger-de Groot, R. E. Poelmann, 2003, "Development-related changes in the expression of shear stress responsive genes KLF-2, ET-1, and NOS-3 in the developing cardiovascular system of chicken embryos," Developmental Dynamics, 230, pp. 57-68.
[50] Groenendijk, B. C. W., S. Stekelenburg-de Vos, P. Vennemann, J. W. Wladimiroff, F. T. M. Nieuwstadt, R. Lindken, J. Westerweel, B. P. Hierck, N. T. C. Ursem, R. E. Poelmann, 2008,

"The endothelin-1 pathway and the development of cardiovascular defects in the haemodynamically challenged chicken embyo," Journal of Vascular Research, 45(54-68).

[51] Kurihara, Y., H. Kurihara, H. Oda, K. Maemura, R. Nagai, T. Ishikawa, Y. Yazaki, 1995, "Aortic arch malformation and ventricular septal defect in mice deficient in endothelin-1," J. Clin. Invest., 96, pp. 293-300.

[52] Waldo, K. L., M. R. Hutson, C.C. Ward, M. Zdanowicz, H. A. Stadt, D. Kumiski, R. Abu-Issa, M. L. Kirby 2005, "Secondary heart field contributes myocardium and smooth muscle to the arterial pole of the developing heart," Developmental Biology, 281, pp. 78-90.

Figure1
Click here to download Figure: Figure1.pptx

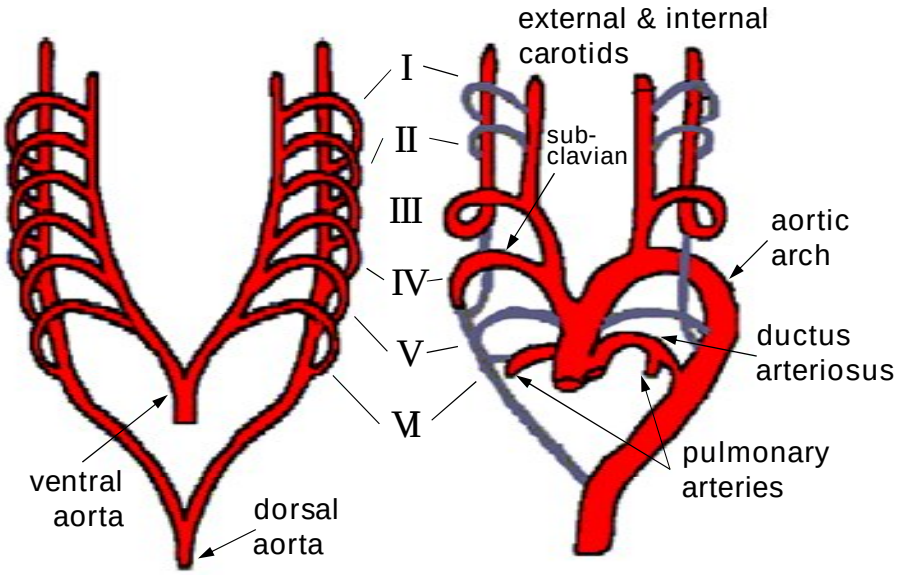

Figure 1: A cartoon representation of all 6 pairs of aortic arch branches that appear, disappear and reappear during early embryonic development. Not all arches exist at the same time, and a general trend occurs where cranial arches are replaced by caudal arch pairs. The sketch on the right hand side shows the association of major arterial great vessels at term with these six aortic arch pairs. Grey solid lines represent the arch vessels that became extinct during development.

Figure2

Click here to download Figure: Figure2.pptx

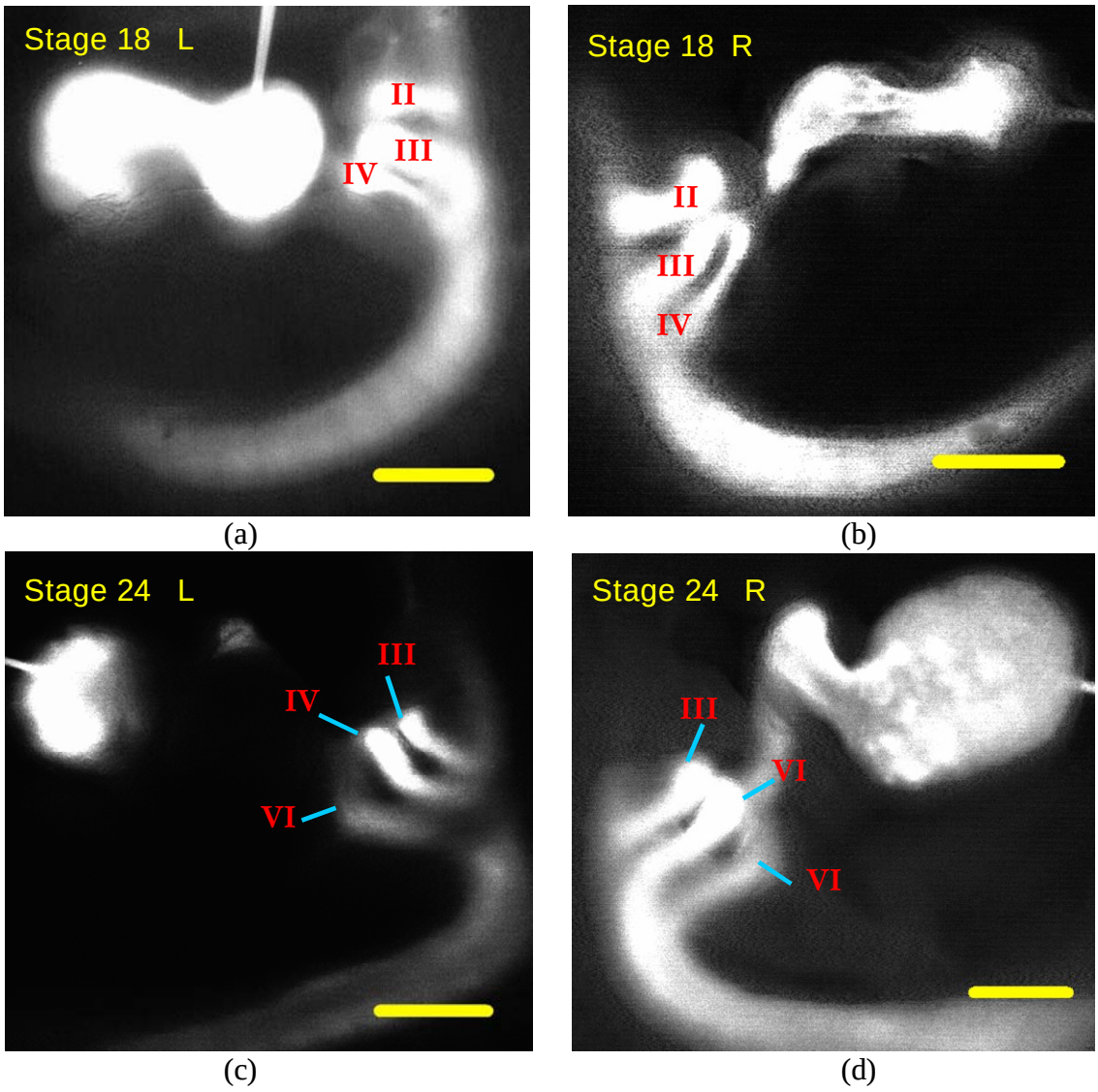

Figure 2: Representative left lateral (a,c) and right lateral (b,d) views of embryonic chick aortic arches with Rhodamine B at Stage 18 (a, b) and Stage 24 (c, d). There are 3 pairs of aortic arches at Stages 18 and 24, but with different patterns. Individual aortic arches are labeled with roman numerals. The scale bar corresponds to 500 µm.

Figure3
Click here to download Figure: Figure_new3(4).pptx

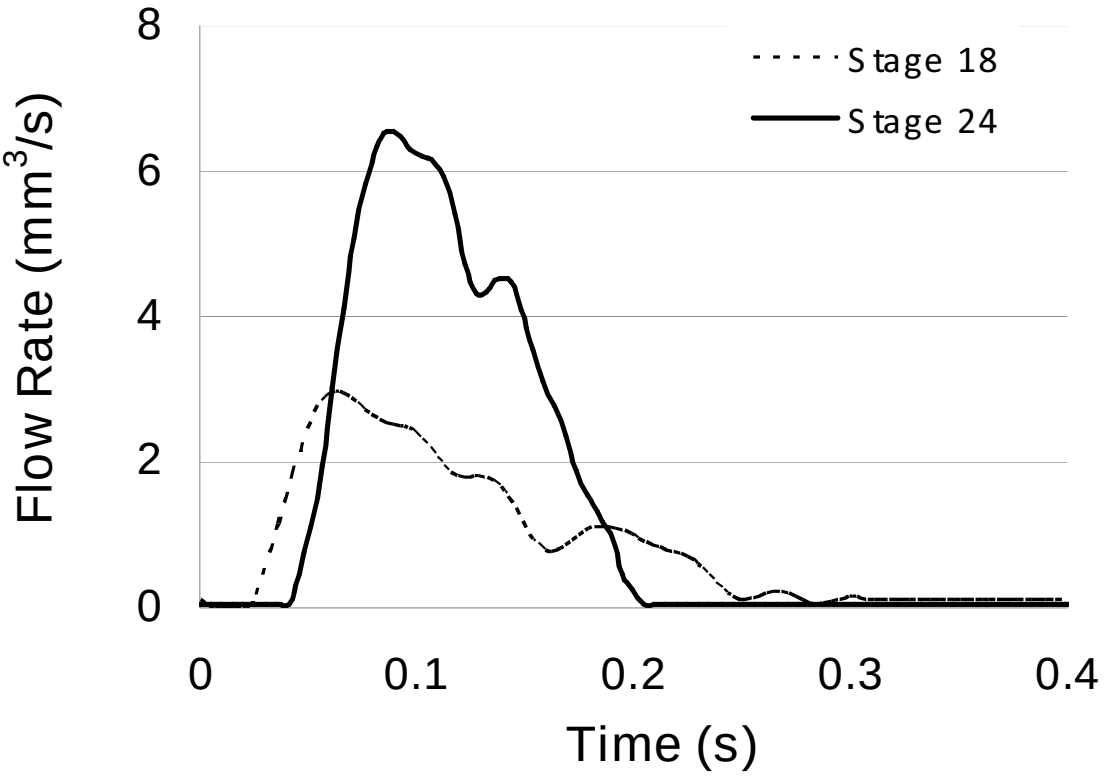

Figure 3: Pulsatile flow rate waveforms used to represent a single cardiac cycle at the inlet to the aortic sac for Stage 18 and Stage 24 models based on the data published by Yoshigi et al. (2000) Ref. [40]. The heart rate is 160 beat per second at Stage 18 and 132 beat per second at Stage 24.

Figure4
Click here to download Figure: Figure_new4(7).pptx

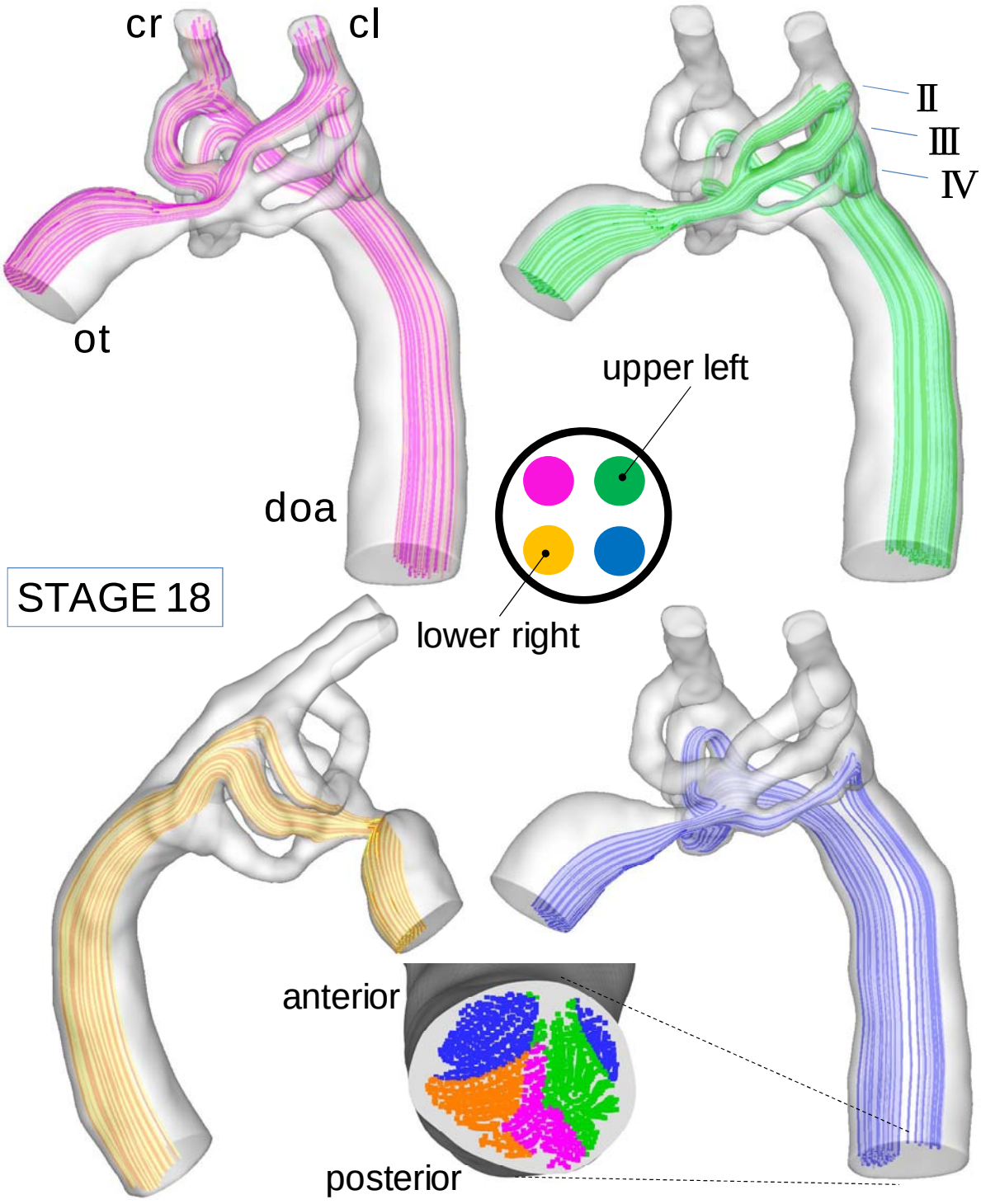

Figure 4: Representative mean flow path-lines at Stage18 of particles released from different inlet quadrants into the proximal aortic sac. Note that flow stream separation was maintained in the aortic sac and each quadrant of inlet flow preferentially filled specific right and/or left aortic arches. Panel a: Right upper quadrant flow or right ventral quadrant flow (pink). Panel b: Left upper quadrant flow or left ventral quadrant (green). Panel c: Right lower quadrant flow or right dorsal quadrant flow (orange). Panel d: Left lower quadrant flow or left dorsal quadrant flow (blue).

Figure5
Click here to download Figure: Figure_new5(8).pptx

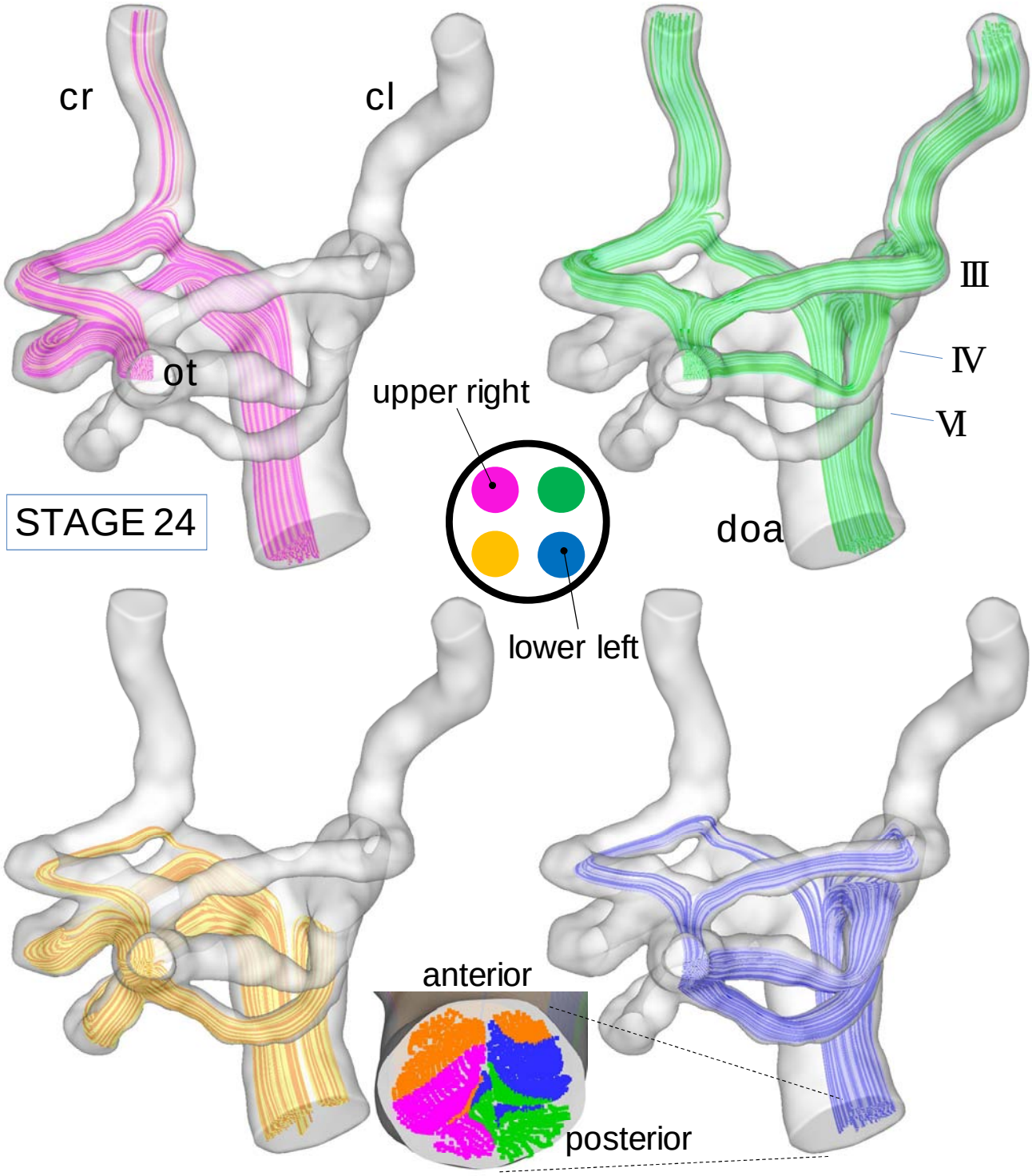

Figure 5. Representative mean flow path-lines at Stage 24 of particles released from different inlet quadrants into the proximal aortic sac. Similar to Stage 18, flow stream separation was maintained in the aortic sac and each quadrant of inlet flow preferentially filled specific right and/or left aortic arches, though the pattern differed from Stage 18 due to disappearance of the IInd aortic arches and appearance of the VIth aortic arches. Panel a: Right upper quadrant flow (pink). Panel b: Left upper quadrant flow (green). Panel c: Right lower quadrant flow (orange). Panel d: Left lower quadrant flow (blue).

Figure6
Click here to download Figure: Figure_new6(9).pptx

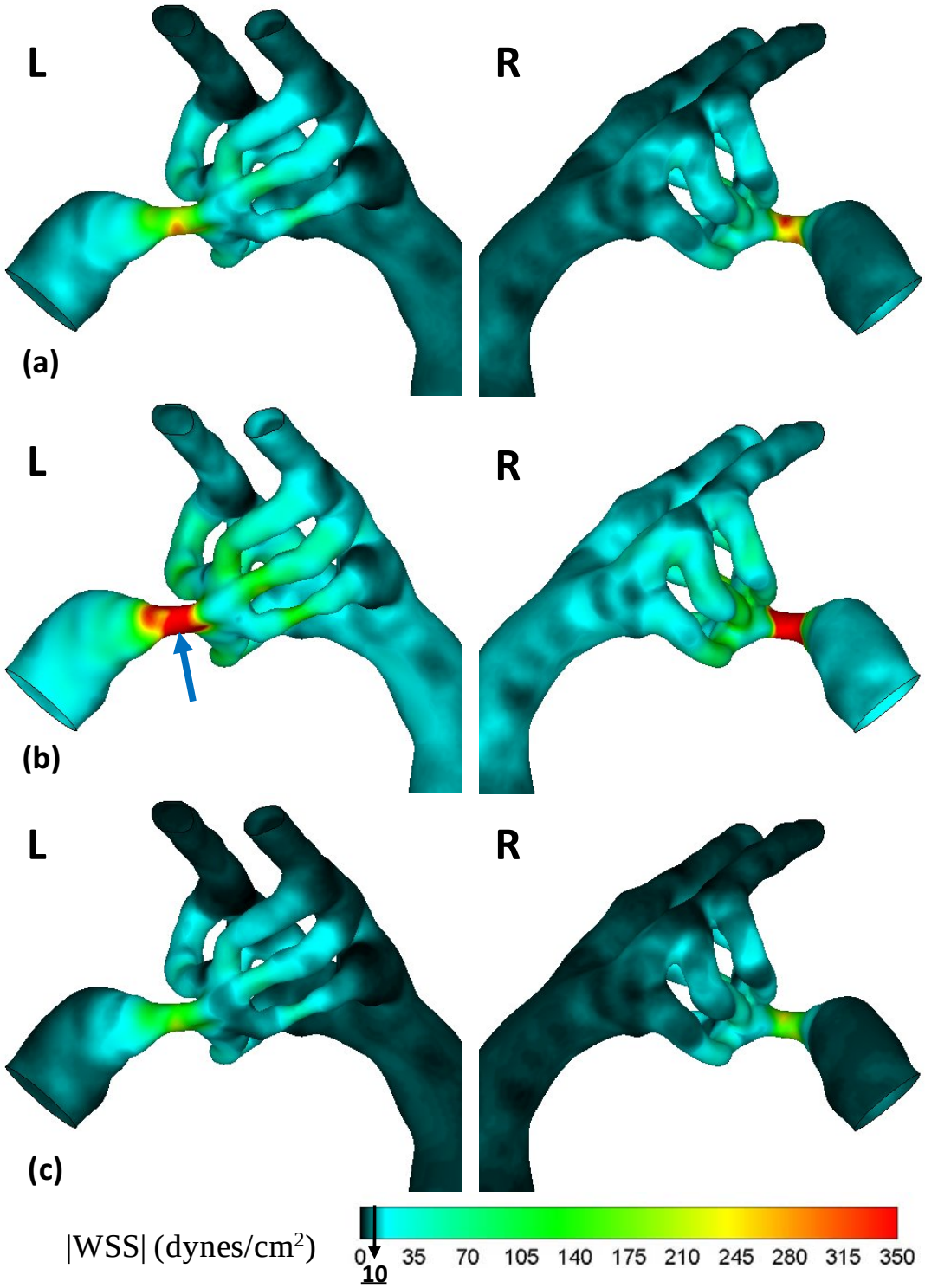

Figure 6: Aortic sac and aortic arch wall shear stress (WSS) distributions at Stage 18 displayed from left lateral (L) and right lateral (R) views. Corresponding to (a) flow acceleration; (b) peak flow velocity; (c) flow deceleration phases of the cardiac cycle. A maximum WSS value of 687 dynes/cm^2 was noted briefly in several distinct areas (see arrow). In order to display a broader range of WSS, a peak WSS of 350 dynes/cm^2 is shown in the legend.

Figure7
Click here to download Figure: Figure_new7(10).pptx

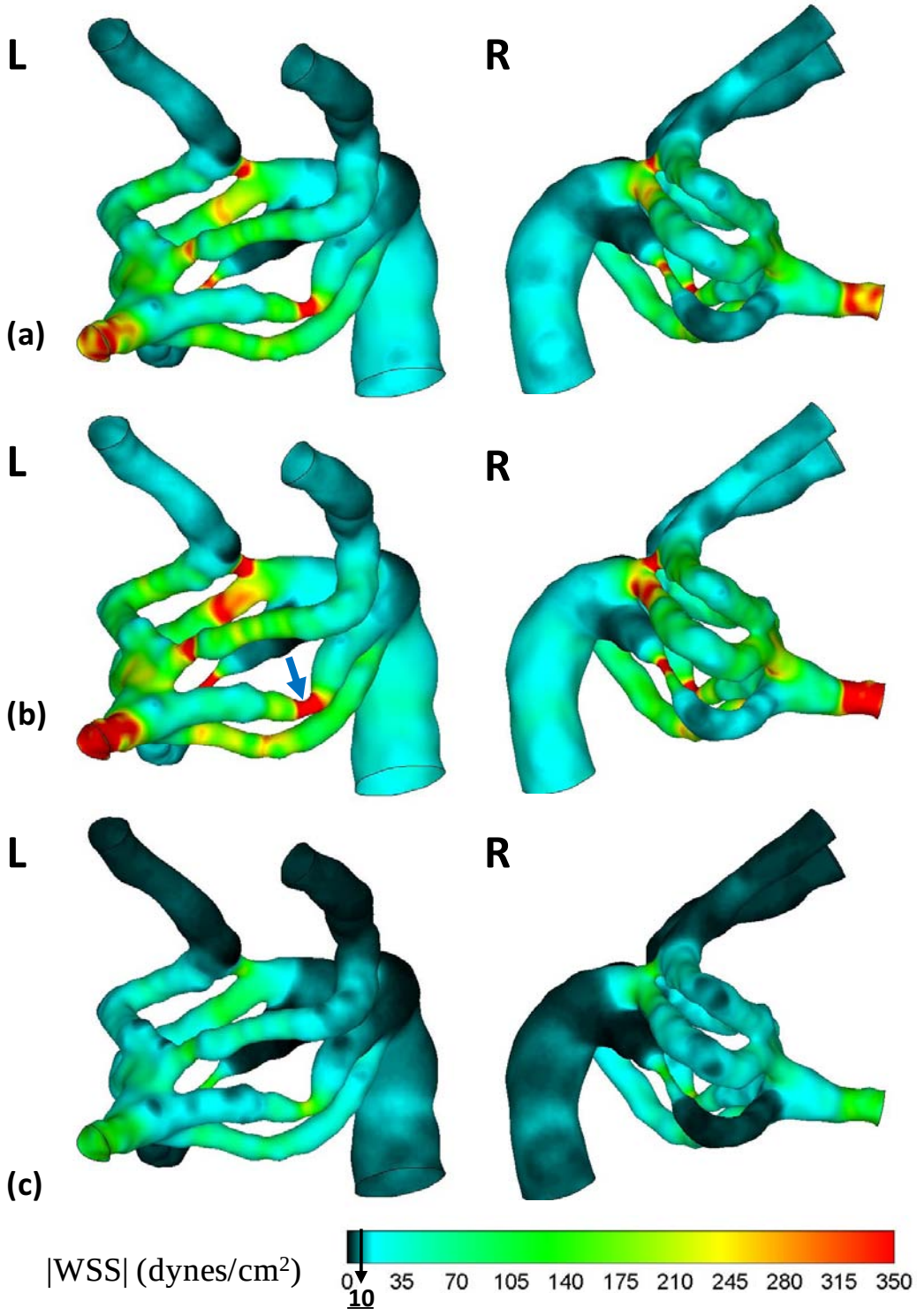

Figure 7: Aortic sac and aortic arch wall shear stress (WSS) distributions at Stage 24 displayed from left anterior oblique (L) and right lateral (R) views. Corresponding to (a) flow acceleration; (b) peak flow velocity; (c) flow deceleration. A maximum WSS value of 720 dynes/cm^2 was noted briefly in several distinct areas (see arrow). In order to display a broader range of WSS, a peak WSS of 350 dynes/cm^2 is shown.

Table

Click here to download Table: Manuscript_Table-1_only_Yajuan_v2-od2.docx

Table 1: Developmental shifts and measurements of the aortic arch mid-point diameters at Stages 18 and 24. L: left; R: right; SD: standard deviation; n: number of samples studied per group. Statistically significant differences ($p<0.05$) in individual arch diameter between stages are denoted by * (arch growth). For fixed arch type, the statistically significant diameter differences between R and L laterals are denoted by † (right dominance). Statistically significant differences from the remaining two arches on the same lateral are indicated by ‡.

Aortic Arch	Lateral Side	Midpoint diameter (±SD) (mm)		N	
		Stage 18	***Stage 24***	***Stage 18***	***Stage 24***
II	L	0.101 ‡ (0.025)	-	33	-
	R	0.112 ‡ (0.021)	-	23	-
III	L	0.127 (0.023)	0.112 * (0.015)	33	24
	R	0.129 (0.037)	0.123 † (0.016)	23	30
IV	L	0.075 (0.011)	0.118 * (0.019)	29	24
	R	0.083 (0.020)	0.140 * † (0.024)	23	30
VI	L	-	0.113 (0.019)	-	24
	R	-	0.138 † ‡ (0.024)	-	29

Table 2: Wall shear stress (WSS) averaged spatially over each aortic arch segment at Stages 18 and 24 for the peak flow condition and averaged over the cardiac cycle (time-averaged); L: left; R: right; SD: standard deviation. The cardiac-cycle averaged WSS at the midpoint of the arches are also provided for comparison with the measured midpoint diameters (Table 1). WSS for individual arch is calculated from the representative CFD model for Stage 18 and Stage 24.

Aortic Arch	Lateral Side	Spatial-average arch WSS (dynes/cm^2)				WSS at arch midpoint (dynes/cm^2)	
		Peak flow WSS (±SD)		Cardiac-averaged WSS (±SD)			
		Stage 18	***Stage 24***	***Stage 18***	***Stage 24***	***Stage 18***	***Stage 24***
II	L	59.4 (14)	-	17.9 (5)	-	32	-
	R	47.1 (12)	-	14.3 (4)	-	24	-
III	L	64.4 (18)	104.9 (37)	19.4 (5)	23.6 (8)	53	45
	R	55.8 (17)	82.2 (16)	17.0 (5)	18.4 (4)	37	40
IV	L	41.7 (17)	92.3 (56)	12.5 (5)	20.8 (12)	49	164
	R	59.9 (18)	122.9 (40)	18.2 (6)	27.5 (9)	33	80
VI	L	-	130.7 (28)	-	29.3 (6)	-	86
	R	-	40.4 (40)	-	9.0 (9)	-	61

Animation Stage 24 Aortic arch particle pathlines

The animation that shows the particle path lines at Stage 24 aortic arch manifold can be downloaded from the following web address:

http://www.andrew.cmu.edu/user/kpekkan/Supplemantal_Movie_Stage24_particle_pathlines.avi

(http://www.andrew.cmu.edu/user/kpekkan/Supplemantal_Movie_Stage24_particle_pathlines.avi)

We could not upload this file to the Editorial Manager as it didn't allowed avi files. Hope all reviewers could see this animation that shows the unsteady flow distribution of quadrant flow streams.